Experimental Studies on Monitoring and Metering of Radial Deformations on Transformer HV Winding Using Image Processing and UWB Transceivers

Shahed Mortazavian, *Student Member, IEEE*, Masoud M. Shabestary, *Student Member, IEEE*, Yasser Abdel-Rady I. Mohamed, *Senior Member, IEEE*, and Gevork B. Gharehpetian

***Abstract*—In this paper, a novel method based on image processing is proposed for detecting the presence and location of mechanical deformations on an actual power transformer winding. A vertical imaging setup is used to obtain a two-dimensional (2-D) image of the transformer winding using synthetic aperture radar (SAR) imaging method and Kirchhoff migration algorithm. The main goal of the image processing method is to detect the location of the radial deformation on the transformer high-voltage (HV) winding. Two different deformations are applied on the winding under the test in this paper. The first one is a modeled bulgy mechanical deformation and the second one is an actual concave buckling made on the actual transformer HV winding. The experimental results for different cases show the effectiveness of the proposed method to detect the presence and location of the deformation on the transformer winding.**

***Index Terms*—Fault diagnosis, fault location, image processing, mechanical deformation, migration algorithm, monitoring and metering, synthetic aperture radar (SAR) imaging, transformer high-voltage (HV) winding, ultrawideband (UWB) transceivers.**

I. Introduction

RECENT YEARS have witnessed the increasing interests, both in research and engineering domains, in the automated fault detection and condition monitoring of electrical equipment with smarter and more efficient approaches. To enhance the reliability of the system, it is necessary to detect, identify, and even predict the faults and failures at early stages as quickly as possible to provide proper remedies. Furthermore, to reduce the amount of unnecessary downtime for maintenance purposes, and consequently reduce important costs in terms of money and time, automated equipment monitoring and fault diagnosis are attracting significant attentions [1]–[3]. Associated with these objectives, numerous noteworthy efforts and novelties have been recently reported in the literature, such as weld defect detection [4], automated inspection of magnetic cores [5], induction machines fault diagnosis [3], [6], [7], and fault diagnosis in power transformers [8]–[17].

Power transformers are critical equipment in the interconnected power grids which may face electrical or thermal disturbances that cause faults such as arcing, partial discharge, and mechanical deformation. Short circuit currents, unsuitable transportation, and gas explosions are known as the main causes of mechanical defects on transformer windings. They can cause radial deformation or axial displacement, tilting, concave buckling, broken clamping parts, and shortened or open turns on transformer windings [12]. If these mechanical faults remain undiagnosed for a long time, they can initiate more severe failures and disrupt power supplies, inducing huge financial losses or causing worst incidents such as explosions, loss of human lives, or environmental disasters [9]. Therefore, to minimize these problems, early-stage detection of internal deformations prior to problematic failures in a transformer is of vital importance. Traditional offline deformation detection [12], [13], frequency response analysis [14]–[16], dissolved gas analysis [9], voltage–current locus [17], and using ultrawideband (UWB) sensors and synthetic aperture radar (SAR) imaging [8], [10], [11] are some of the recently proposed transformers monitoring methods in the literature. There are substantial advantages in online monitoring methods. They do not affect the transformer operation to get the desired data, leading to save huge outage costs. Furthermore, online monitoring methods are vital in terms of the prognosis of major faults before occurring by detecting their initial signs in early development stages. Therefore, it can prevent possible huge damages during operation and increases system reliability.

In [11], an online method has been introduced which uses SAR imaging and UWB transceivers. Since the UWB technology has high data transmission rate, low cost, and very low power consumption, it is appropriate to be used in many industrial applications [18] such as current measurements in power electronics or in electromagnetic interference domains [19]. Reference [11] shows the feasibility of using UWB sensors and SAR imaging in detecting the presence of some modeled radial deformations on a modeled winding. However, this method has not been applied on an actual transformer winding with actual deformations. Besides, the capability of the mentioned method to detect the location of the mechanical deformation along the transformer winding has not been studied. Also, the practicability of the application of the UWB monitoring method on actual transformers in an online manner has not been addressed

Manuscript received October 14, 2014; revised December 26, 2014, February 09, 2015, April 11, 2015, June 19, 2015, July 25, 2015, and August 30, 2015; accepted August 31, 2015. Date of publication September 17, 2015; date of current version December 02, 2015. Paper no. TII-14-1135.

S. Mortazavian, M. M. Shabestary, and Y. A.-R. I. Mohamed are with the Department of Electrical and Computer Engineering, University of Alberta, Edmonton, AB, T6G2V4, Canada (e-mail: shahed1@ualberta.ca; masoud2@ualberta.ca; yasser2@ualberta.ca).

G. B. Gharehpetian is with the Department of Electrical Engineering, Amirkabir University of Technology, Tehran, 15914, Iran (e-mail: grptian@aut.ac.ir).

Color versions of one or more of the figures in this paper are available online at http://ieeexplore.ieee.org.

Digital Object Identifier 10.1109/TII.2015.2479582

in the literature. Also, there is a lack of an analytical approach to detect the presence of the deformation in [11], since it only applies schematic comparisons. This, in turn, causes substantial limitations for further useful analysis.

The main motivations behind this paper are as follows:

1) modifying the method presented in [11] to detect the presence of the deformation in an analytical and quantitative manner;
2) applying the proposed method on actual deformations in actual transformer windings;
3) locating different bulgy and concave deformations using the proposed quantitative analytical method;
4) discussing the practicability issues of the proposed ideas to be adopted by industry.

A two-dimensional (2-D) image of the transformer winding is obtained via SAR imaging procedure using UWB sensors and Kirchhoff migration (KM) algorithm. This method is an accurate way in detecting the location of the deformation. Also, it is faster than the method suggested in [20], and more importantly, it can be used online to locate the deformation without huge computational burdens. Hereinafter, the word "winding" refers to the high-voltage (HV) winding, unless otherwise stated.

The experimental results on six modeled and actual deformations are presented to show the effectiveness of the proposed method. The results show that these methods are capable of detecting the location of the deformations on transformer windings. Since making an actual deformation on a winding is a nonreversible process, in the first five test cases, a mechanical deformation model is used to provide the possibility of changing the location of the deformation along the transformer winding. Finally, the capability of the proposed method in detecting an actual buckling radial deformation is studied and experimental results are provided. All results show the effectiveness of the proposed method in detecting different mechanical deformation locations on the transformer winding.

II. SAR Imaging and KM Algorithm

The schematic figure of the SAR imaging setup is shown in Fig. 1, in which a transceiver generates a pulse, and the pulse is transmitted through transmitting antenna (TA) to the environment. When the transmitted pulse meets the target, a portion of it reflects back to the receiving antenna (RA). This is a one-dimensional (1-D) signal carrying some information about the target. More impulse responses from other positions thoroughly help to obtain more information from the target. Therefore, the antennas are moved in a specific direction called movement route. The process of transmitting and receiving signals is repeated at predefined points along the movement route to obtain several impulse responses called "scans." For simplicity, the distance between adjacent measuring points or steps is set to be constant. The set of all scans forms a 2-D matrix, which is a function of the time and measuring positions. The process to form a 2-D picture from these scans is thoroughly explained in [21].

The typical UWB pulse of the UWB transceiver, which is used in this paper, is shown in Fig. 2. It is a Gaussian pulse modulated by a sinusoidal carrier. After the alignment

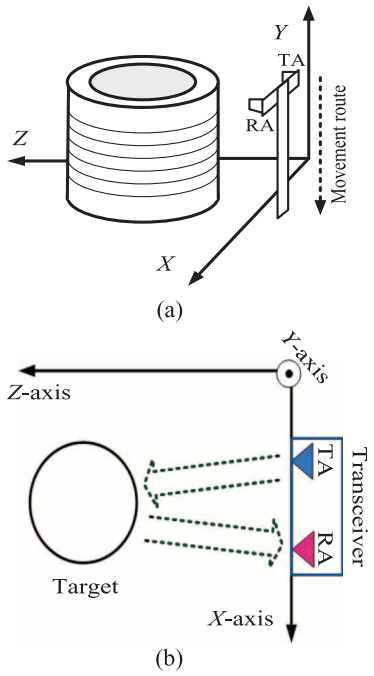

Fig. 1. SAR imaging method. (a) 3-D scheme. (b) Top view.

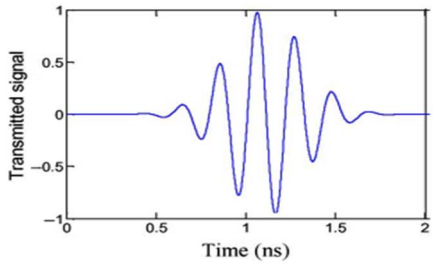

Fig. 2. UWB pulse [22].

procedure of scans, undesired parts can be removed from the raw impulse response. For this three-dimensional (3-D) target, there are several paths through TA-target-RA. The closest point of the target to the antennas provides the shortest path with minimum transmission time ($T_{\min}$) and the farthest point makes the longest path ($T_{\max}$). Therefore, the time delay of the target reflection is t as $T_{\min} \leq t \leq T_{\max}$. Discussions and calculations of how to improve the resolution of the test system are presented in detail in [22]. After preprocessing steps, the scans are ready to be used by the migration algorithm to form a 2-D image. The Kirchhoff integral method introduces a quantitative statement of the Huygen principle and obtains lower sidelobe level and significantly higher quality image. The Helmholtz–Kirchhoff integral theory describes the inverse problem of the electromagnetic propagation as migration. Since the KM treats electromagnetic waves as scalar waves, it can neglect all depolarization phenomena. In this paper, antennas are considered to be isotropic. The Kirchhoff approximation is also one analytical approximation method which can simply calculate the scattering from a rough surface [22]. According to the Kirchhoff integral theory, if there is a Green function (Γ) with the boundary condition determined on the surface $z = 0$, boundary $\partial\Omega$ can be taken to consist of the plane $z = 0$ smoothly joined to a

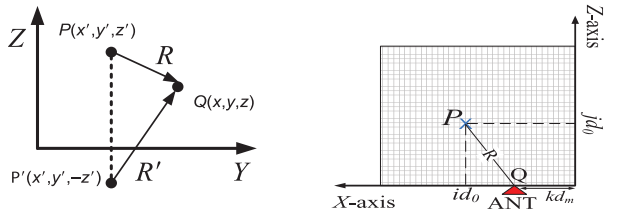

(a) (b)

Fig. 3. (a) Source and observation points of Green function. (b) Implementation of KM equation.

large hemisphere. Therefore, the integral of the surface can be written as follows:

$$\forall r \in \Omega : U(r,t) = -\frac{1}{4\pi}\int_0^{\infty}\left[\int_{S1} f(r',t')\,\partial_n\Gamma(r,t,r',t')\,ds + \int_{z'=0} f(r',t')\,\partial_n\Gamma(r,t,r',t')\,ds\right]dt' \tag{1}$$

where $r'$and t' are source coordinates; r and t are supposed to be the observer coordinates of the Green function. ds is the differential element on $\partial\Omega$. $\partial_n\Gamma$ is the normal continuous derivative of the Green function. S_1 represents the hemisphere. If the wave velocity v is constant in the medium, the radius of the hemisphere can be increased to infinity. In [23], it is shown that in this situation, the first integral in (1) over S_1 can be assumed to be zero. Therefore, the Γ should be zero over the plane $z = 0$. Now, a Green function should be found that suits the condition of the Kirchhoff integral which is zero over the boundary. In the assumed conditions, two Γs, which vanish over the plane $z = 0$, are calculated by the method of images and the anticasual Green function is selected [22]. Fig. 3(a) shows the related parameters of this function. By substituting the Green function in Kirchhoff integral of (1), after required manipulations, and modifying the relation from 3-D space to 2-D case (by simply eliminating the dimension of Y-axis), one reaches

$$U(r,t) = \frac{1}{2\pi}\frac{\partial}{\partial z}\int \frac{f\left(x', t+\frac{R}{v}\right)}{R}\,dx' \tag{2}$$

where r can be any point on the X–Z plane. This equation is the Schneider's KM equation. However, the surface integral has reduced to a line integral and the plane $z = 0$ has decreased to the X-axis, in the case studied in this paper. Now, the boundary conditions on X-axis should be determined. Equation (2) can be considered as a mapping from space of possible boundary conditions to wave equation solutions [11]. In the SAR imaging process, the wave travels from the TA to the target and reflects back to the RA. The total wave travel time would be almost twice the travel time from the target to the observation point RA. The magnitude of the reflected wave from every point of the target on the plane is calculated as follows:

$$U(x,z) = \frac{1}{2\pi}\frac{\partial}{\partial z}\int \frac{f\left(x', 2\frac{R}{v}\right)}{R}dx'. \tag{3}$$

The total energy radiated from the X–Z plane can be achieved by 2-D function of $U(x, z)$. The edges of the target, i.e., the transformer winding in this paper, will be illustrated by plotting $U(x, z)$ in the X–Z plane. If $g_k(nT_s)$ represents the kth scan in which k, $n = 0, 1, 2, 3, \ldots$ and T_s is the scanning sample time, the discrete boundary condition can be written as follows:

$$\forall k,\ n \in N \quad f(kd_M, nT_s) = g_k(nT_s) \tag{4}$$

where d_M is the distance between two neighboring measured points and kd_M is the coordinate of the kth measured point on the X-axis. The KM equation in the discrete boundary condition is shown in Fig. 3(b). The $P(id_0, jd_0)$ is an arbitrary point in which the magnitude of the image function is calculated. $Q(kd_M,\ 0)$ is the antennas location, where d_0 is the special step and

$$i, j, k \in Z \quad \text{and} \quad 0 \le i < M,\ 0 \le j < N,\ 0 \le k < K \tag{5}$$

where M and N show the number of image pixels on the X- and Z-axes and K is the total number of measured points. In addition, $U(x, z)$ should be changed into a discrete form. To do so, the continuous variables x, z, x', and t should be replaced by discrete ones, i.e., id_0, jd_0, kd_M, and nT_s, respectively. Furthermore, the integral should be substituted by the summation and the derivative by the difference. So, the discrete form is as follows:

$$U(id_0, jd_0) = U(id_0, jd_0) + \frac{d_M \cdot jd_0}{2\pi \cdot R^2 \cdot v \cdot T_s} \times \sum_k \left[f(kd_M, (n+1)T_s) - f(kd_M, nT_s)\right]\Big|_{nT_s = 2R/v}. \tag{6}$$

By depicting the image function output on the X–Z plane, the final image of transformer winding edges will be obtained.

III. Vertical Imaging Setup

It should be mentioned that the horizontal setup presented in [11] is not practically installable on a transformer tank due to its required length which is almost twice the required length of vertical setup and almost three times bigger than the available width on the tank of the transformer in this paper, as shown in Fig. 4. However, the required length for the vertical imaging setup can be as low as the height of the tank as also illustrated in Fig. 4. Therefore, the vertical setup is generally more practical from the point of view of transformer manufacturers. In this setup, the imaging route in front of the transformer winding is vertical as demonstrated in Fig. 4(a). In this setup, the measurement steps are 24 points. The mechanical deformation model is made up of copper strips with the dimensions illustrated in Fig. 4(b). In different test cases, the radial deformation model is placed in three different heights of the transformer winding,

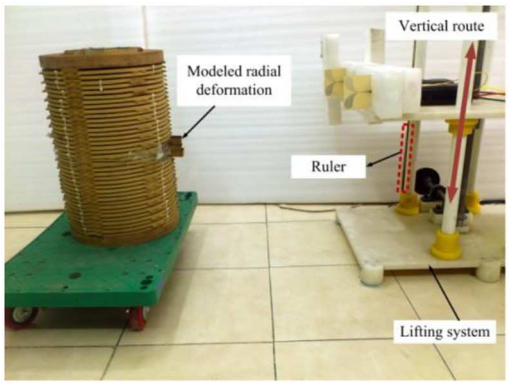

(a)

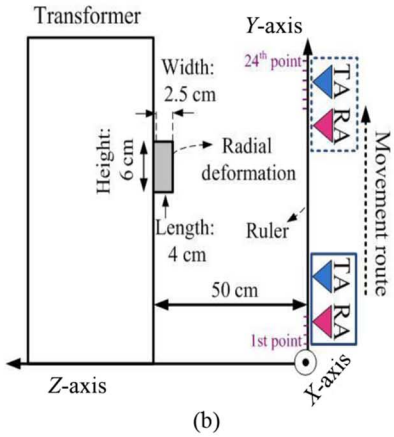

(b)

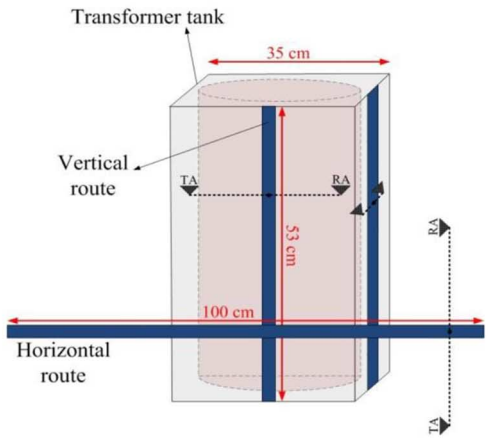

(c)

Fig. 4. Test setup. (a) Experimental setup. (b) Side view. (c) Horizontal imaging setup versus vertical setup.

as shown in Fig. 5. The length of this deformation is 6 cm and it covers six winding discs in each position. The radial deformation is placed at the "bottom part" (located 7 cm from the bottom of the transformer winding), "middle part" (25 cm from the bottom of the winding), and "top part" (40 cm from the bottom of the transformer winding).

IV. Image Processing Method

The goal of applying image processing methods on the resulted images is to quantitatively detect the presence and the location of the radial deformations on different heights.

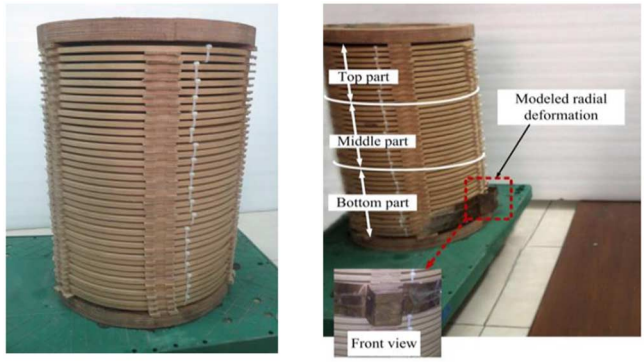

(a) (b)

Fig. 5. (a) Actual transformer winding. (b) Three studied parts for applying mechanical deformation.

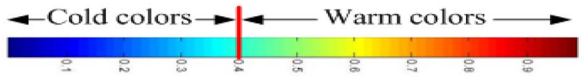

Fig. 6. Color bar and areas of warm and cold colors.

First, the imaging process is applied on the sound transformer winding, which does not have any defect. This image gives a reference as the sound winding image (SWI) for later comparisons. The images reveal a top view of the transformer winding. The warm colors in each image present a high reflection and the cold ones illustrate a moderate reflection from the target. Therefore, the highest reflection occurs from the most front part of the transformer winding because it has the shortest distance from the antennas. Since this method works based on the imaging data received from different heights of the transformer winding, just the vertical imaging setup results are useful for the mentioned purposes.

In this paper, the value of the image pixels is used. The color bar graph in Fig. 6 shows the mapping basis used in this paper which maps each color to a normalized image value between 0 and 1. Hereinafter, these values will be called color number (CN). A simple way to distinguish between warmer and colder colors is to assign a user-defined distinguishing CN (DCN). For a desired accuracy, this DCN should be neither too high (close to 1) nor too low (close to 0). A suitable range for the DCN is between 0.3 and 0.5 as it has been concluded by a trial and error procedure. In this study, a fixed value of 0.4 is selected for the DCN. Knowing this, two different quantities can be defined to give a better understanding of the images: the number of warm color pixels N_{warm} and the summation of the CNs of warm color pixels S_{warm} in each image. These parameters can be used for detecting the presence and (more importantly) the location of the deformations. However, it is shown in the experimental results that, for precise detection of the defect location, it is better to consider both parameters and not rely on just one of them. The SWI is a basis for the comparison and evaluation of defected winding images (DWIs). Image correlation methods are useful approaches introduced in the literature and applied for different purposes [3], [5]. In this paper, imaging data are divided into different sections, and different sections of the SWI are subtracted from the corresponding sections of DWIs

TABLE I
QUANTITATIVE VALUES OF IMAGES TAKEN FROM THE SOUND WINDING

Cases	N_{warm}	Cases	N_{warm}
SWI-1	111908	SWI-3	112051
SWI-2	111439	SWI-4	111343
Average value	**111 685 (=$N_{\text{warm-ref}}$)**	Standard deviation	**347**

as a simple correlation method to monitor the deformation. The result of the correlation represents differences between DWI and SWI including the difference in color or in the shape of their image since the mechanical deformation causes some disorders in DWIs compared to the SWI. Different tests have been examined with different modeled deformations in different locations. Almost in all of these tests, the results are similar and successful. However, to make reviewing the results easy, some of the selected tests and results will be presented in the next section. Also, the proposed methods have been tested successfully on an "actual deformation" (with small and unexaggerated sizes and real shape shown in Fig. 17) for the first time.

A. First Stage: Detecting the Presence of the Deformation

N_{warm} and S_{warm} are quantitative values useful to: 1) quantitatively interpret the qualitative images; 2) distinguish between the sound and defected situations; and more importantly, 3) find the location of the deformation. Since the proposed image processing methods are based on the comparison between the images of the sound and deformed windings, these methods can be applied to any other setting. It means that, for each specific setting, reference images for each side of the windings as SWIs can be obtained. These SWIs are used as signatures or references for that specific transformer. To reduce measurement errors, the average of N_{warm} values for different SWIs can be computed to obtain $N_{\text{warm-ref}}$. The same averaging can be computed for S_{warm} values of different SWIs to obtain $S_{\text{warm-ref}}$. Then, these reference values will be compared to the values of images obtained for other situations. If there is no deformation in kth image, the $N_{\text{warm-k}}$ and $S_{\text{warm-k}}$ values will be very close to their values for the SWIs (i.e., $N_{\text{warm-ref}}$ and $S_{\text{warm-ref}}$). However, for any deformation in any location, ith image will be different from the reference SWIs. Consequently, the quantitative values in the ith test case (i.e., $N_{\text{warm-i}}$ and $S_{\text{warm-i}}$) will be different from $N_{\text{warm-ref}}$ and $S_{\text{warm-ref}}$. Four SWIs have been obtained from the sound transformer winding, and their N_{warm} values are illustrated in Table I. Table I also shows the average of N_{warm} values which also gives the value of $N_{\text{warm-ref}} = N_{\text{warm-average}} = 111\ 685$ (the same procedure can be accomplished to determine $S_{\text{warm-ref}}$). Then, using (7), the distance of N_{warm} value of each image from the $N_{\text{warm-ref}}$ can be obtained to monitor the deformation

$$\Delta N = N_{\text{warm}} - N_{\text{warm-ref}}. \tag{7}$$

To distinguish between sound and defected situations, assigning a threshold is very important. This threshold should be proven to be valid under different deformations and settings. To find a reasonable threshold, the standard deviation of the N_{warm} values for the sound conditions is calculated. According to Table I, the standard deviation of N_{warm} values of sound conditions ($\delta_{N_{\text{warm-SWI}}}$) is 347. Then, (8) can be used to determine the threshold value

$$|\Delta N|_{\text{Thresh}} = \delta_{N_{\text{warm - SWI}}} \times h = 347 \times h. \tag{8}$$

According to the normal distribution curve, the possibility of the occurrence of a value with a distance from the average value more than three times the standard deviation is less than 0.3%. Therefore, the distance of five standard deviations is a conservative range which assures the user with a very high probability that the values out of this range do not represent the sound condition. Thus, $h = 5$ is selected

$$|\Delta N|_{\text{Thresh}} = 347 \times 5 = 1735 \tag{9}$$

which means that the images with $|\Delta N|$ greater than $\Delta N_{\text{Thresh}} = 1735$ most probably contain a deformation. Note that this threshold directly depends on the selection of the DCN. Therefore, 1735 is an obtained threshold value where the DCN is selected 0.4 and the standard deviation of N_{warm} values of the sound winding is 347. This threshold will be different if another DCN value is selected. The proposed ideas of this stage are represented correspondingly in the flowchart in Fig. 7.

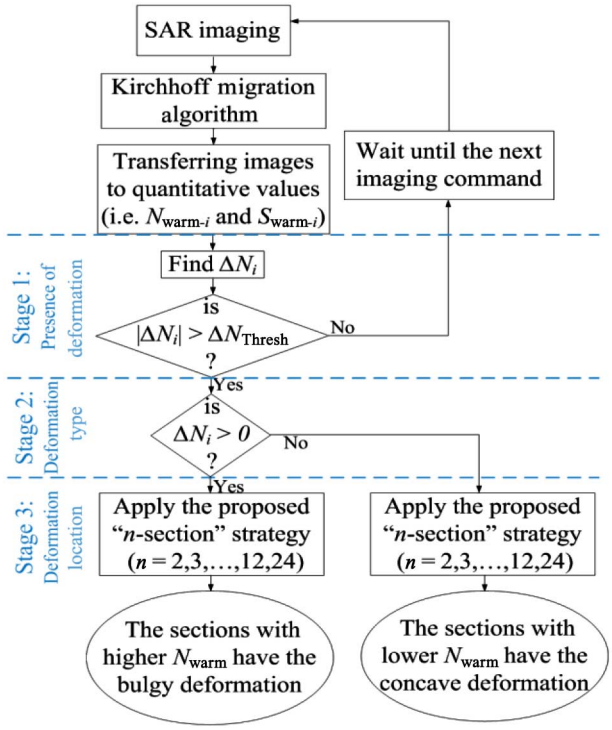

Fig. 7. Flowchart of the proposed ideas.

B. Second Stage: Detecting the Type of the Deformation

After detecting the presence of the deformation in the first stage, the type of the deformation can be determined in the second stage. If the $N_{\text{warm-i}}$ value is greater than the $N_{\text{warm-ref}}$ value, it shows that a bulgy deformation has occurred. As stated

TABLE II
CHARACTERISTICS OF UWB TRANSCEIVERS

Pulse repetition frequency	9.6 MHz
Center frequency	4.7 GHz
Bandwidth	3.2 GHz
Time interval between scans	20 ms

in Section III, this is due to the fact that the highest reflection occurs from the closest part of the transformer winding, and it consequently causes the images of the bulgy deformation to have more warm colors. On the other hand, if the $N_{\text{warm-i}}$ value is smaller than the $N_{\text{warm-ref}}$ value, it represents a concave deformation. The sign of ΔN can also characterize this detection, and positive ΔN represents the bulgy deformation as demonstrated in Fig. 7.

C. Third Stage: Detecting the Location of the Deformation

In the third stage, the information from the antenna (which has been obtained from 24 points in this paper) is divided into n sections where n can be 2, 3, 4, 6, 8, 12, or 24. Depending on the required accuracy, the operator can choose either two-section comparison (to simply detect that the deformation is on the upper or lower sections of the winding) or 24-section comparison (for higher accuracy). After dividing the information of the defected winding into n sections, the information of each section of the deformed winding is investigated to find the deformation location which will be discussed more in experimental results.

V. EXPERIMENTAL RESULTS

The UWB transceivers model is PULSON 220 with characteristics listed in Table II. Also, two microstrip Vivaldi antennas are used as shown in Fig. 8(a). They are used as the TA and RA. The GUI interface software named "bistatic radar" is used to connect the PC to the transceivers and receive the collected data from antennas. KM provides the 2-D images from the data obtained from SAR imaging. Also, the data are normalized to lie in the range between 0 and 1.

A. Detecting the Presence of the Deformation

In this section, one actual and five modeled deformations have been tested to verify the capability of the proposed idea in detecting the presence of the deformation. The locations of these deformations are indicated in Fig. 8(b). In this section, the presence of the deformation is detected based on the comparison of N_{warm} values of DWIs with $N_{\text{warm-ref}}$ using (7). Table III presents the values of N_{warm} and ΔN for each test case. In all defected situations, the values of $|\Delta N|$ is greater than the obtained $\Delta N_{\text{Thresh}} = 1735$. Therefore, this stage is successfully capable to simply detect the presence of the deformation. However, the results of this stage only determine the presence of the deformation, and they do not give information about the location of the deformation. Detecting the location of the deformations will be examined using "n-section" strategies (with $n = 2,\ 3,$ and 12) in the next sections.

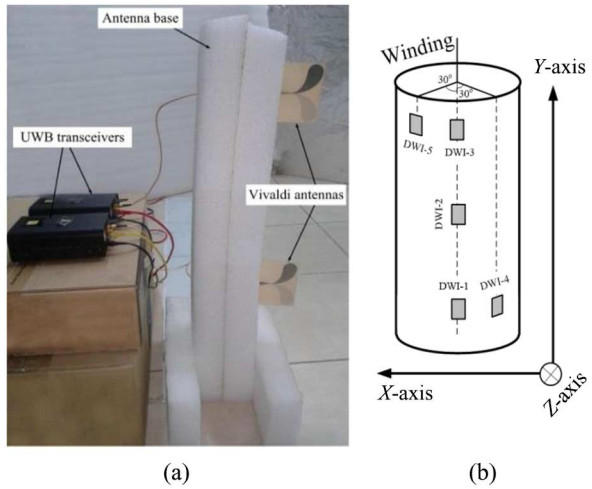

Fig. 8. Experimental setup. (a) Radar imaging setup. (b) Deformation cases.

TABLE III
N_{warm} AND ΔN VALUES OF DIFFERENT IMAGES TAKEN FROM DEFECTED SITUATIONS (NOTE: $N_{\text{warm-ref}} = 111\,685$ AND $\Delta N_{\text{Thresh}} = 1735$)

Cases	Description	N_{warm}	ΔN
DWI-1	Bulgy modeled deformation on bottom-center	116 487	4802
DWI-2	Bulgy modeled deformation on middle	114 980	3295
DWI-3	Bulgy modeled deformation on top-center	124 182	12497
DWI-4	Bulgy modeled deformation on bottom-right	114 614	2929
DWI-5	Bulgy modeled deformation on top-left	118 233	6548
DWI-6	Concave actual deformation on top-center	104 908	−6777

B. "Two-Section" Strategy

In this strategy, the data of each image are divided into two sections: upper section and lower section. In these tests, there are 24 measuring points in the vertical setup; therefore, the upper section image is made up of the data of 12 upper measuring points and the lower section image is made up of the data of 12 lower measuring points. The SWI and all of DWIs are divided in this manner. Figs. 9 and 10 present the resulted images (before applying the correlation) of the lower and upper sections used in the test cases of this strategy in which the mechanical deformation is on the bottom and top parts, respectively. As figures show, it is impossible to visually compare the sound and defected sections in each case and come to a useful conclusion. Therefore, the comparison between quantitative values seems to be necessary. To obtain the correlation, the SWI is simply subtracted from the DWIs. Then, the results are compared to detect the location of the deformation. The subtraction of each section of the SWI from the same section of DWIs is calculated. Then, N_{warm} and S_{warm} values of the correlated images are computed. Table IV demonstrates the N_{warm} and S_{warm} values of this strategy. For instance, when the deformation is on the top, the N_{warm} for the correlated image of the upper and lower sections are 28 171 and 22 384, respectively, which shows a higher N_{warm} in upper section. On the other hand, when the deformation is on the bottom, the N_{warm} value for the correlated image of the lower section is higher than that of the upper section. It is concluded that this strategy is capable

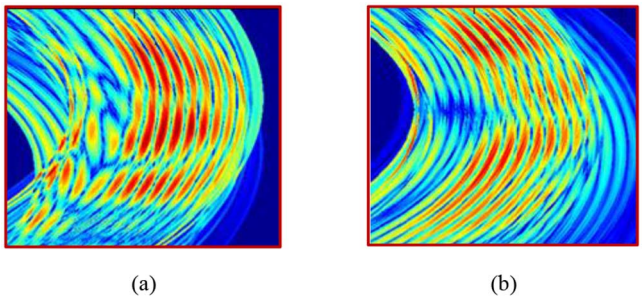

Fig. 9. "Two-section" strategy applied on imaging data of winding when deformation is on bottom part. (a) Lower section. (b) Upper section.

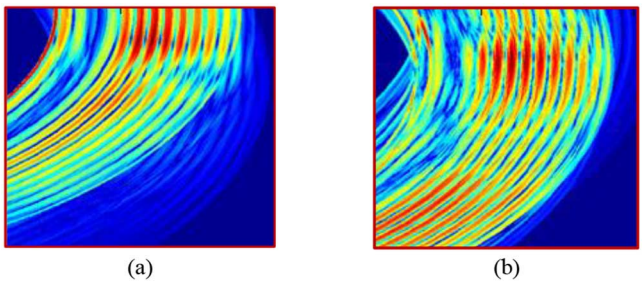

Fig. 10. "Two-section" strategy applied on imaging data of winding when deformation is on top part. (a) Lower section. (b) Upper section.

TABLE IV
QUANTITATIVE VALUES FOR "TWO-SECTION" STRATEGY

Cases		N_{warm}	S_{warm}
Deformation on bottom part	Upper section	27178	12427
	Lower section	**28344**	**14599**
Deformation on top part	Upper section	**28171**	**11074**
	Lower section	22384	9838

of detecting the location of the deformation. The same conclusion can be made based on the values of S_{warm} in correlated images which are similarly indicated in Table IV. Considering that the imaging data are divided into upper and lower sections, only the deformations in the bottom part and top part of the winding can be detected in this strategy.

C. "Three-Section" Strategy

This strategy is similar to the two-section strategy, but each image data is divided into three sections: lower section, middle section, and upper section. The image of each section is the result of the data from eight measuring points. Fig. 11 presents the images obtained for the three sections when the deformation is in the middle part. Also, Table V illustrates the quantitative results of three-section strategy for three test cases. For example, when the deformation is in the middle part of the winding, the highest N_{warm} and S_{warm} are 37 271 and 17 582, respectively, which both correspond to the middle section. S_{warm} of upper and lower sections are 10 318 and 11 122, respectively, and both of them are lower than S_{warm} in the middle section. Therefore, in each test case, the location of the deformation is detected where the defected section has higher N_{warm} and S_{warm} values.

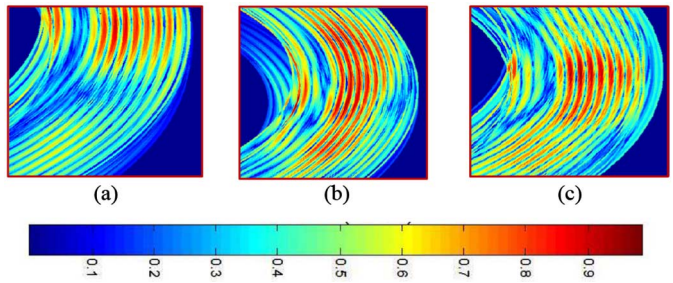

Fig. 11. "Three-section" strategy when deformation is on middle part. (a) Lower section. (b) Middle section. (c) Upper section.

TABLE V
QUANTITATIVE VALUES FOR "THREE-SECTION" STRATEGY

Cases		N_{warm}	S_{warm}
Deformation on bottom part	Upper section	33619	15005
	Middle section	36907	15838
	Lower section	**45840**	**21258**
Deformation on middle part	Upper section	21909	10318
	Middle section	**37271**	**17582**
	Lower section	21880	11122
Deformation on top part	Upper section	**38411**	**18895**
	Middle section	33015	16110
	Lower section	28250	14182

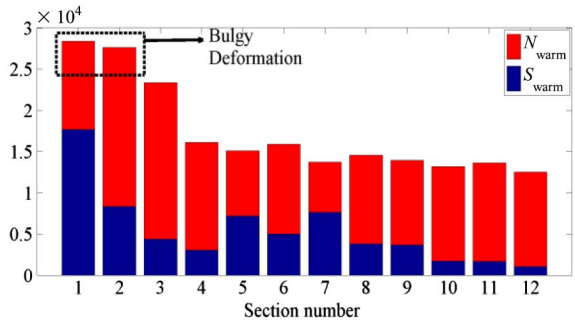

Fig. 12. "12-section" strategy results for deformation on bottom-center.

D. "12-Section" Strategy

The previous sections showed that the accuracy of the proposed ideas in detecting the deformation location is increased by increasing the correlated sections. In this strategy, the number of sections is increased to 12 which means that each section includes the data from two measuring points. Therefore, the SWI and each DWI are divided into 12 sections and the correlations between pairs are obtained. Since the number of pictures is higher than before, the quantitative results are presented in bar graphs to make a sensible and better comparison. Fig. 12 shows the results for the case of deformation on the bottom part. Red bars show N_{warm} value in each section and the blue bars represent corresponding S_{warm}. It is clear that both parameters are higher for the first two sections. As Fig. 12 shows, the proposed ideas successfully found the location of the mechanical deformation on transformer winding with a higher accuracy in comparison to the previous strategies. Figs. 13 and 14 show the similar results for test cases where

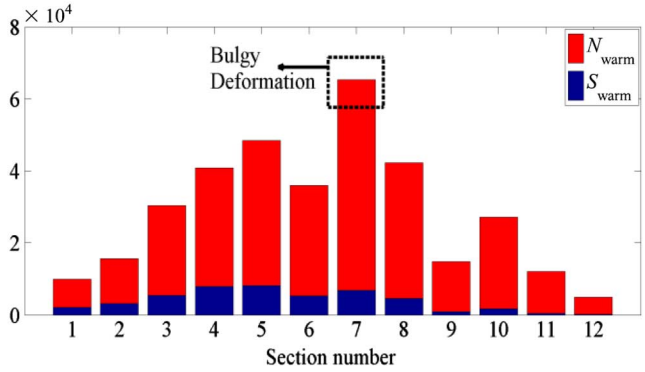

Fig. 13. "12-section" strategy results for deformation on middle-center.

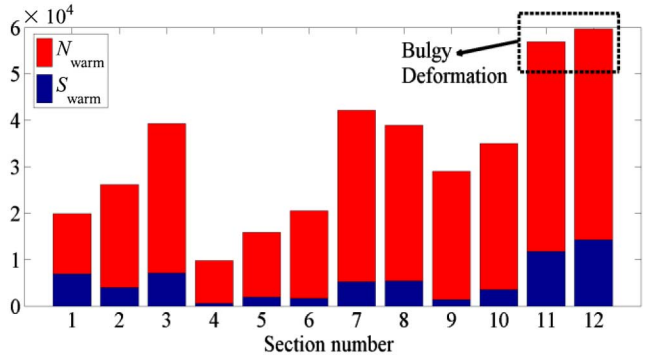

Fig. 14. "12-section" strategy results for deformation on top-center.

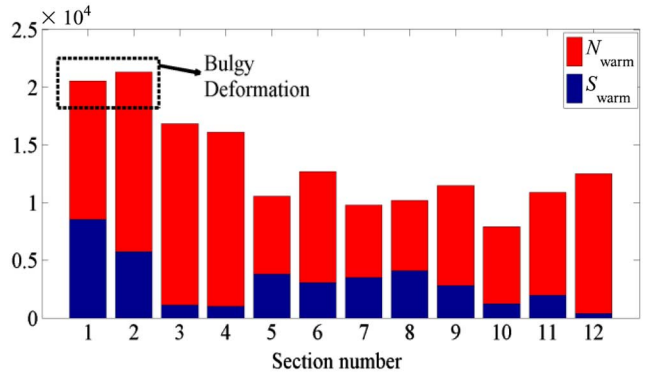

Fig. 15. "12-section" strategy results for deformation on bottom-right.

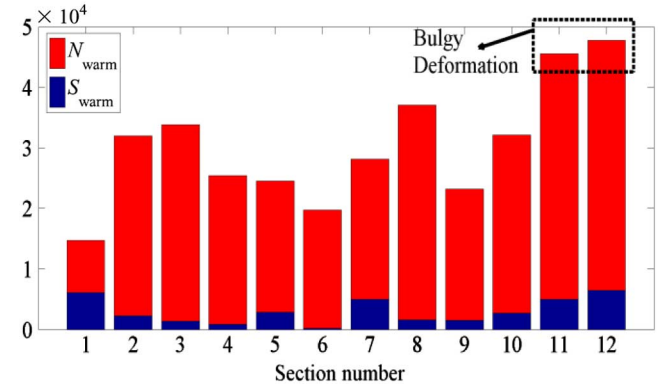

Fig. 16. "12-section" strategy results for deformation on top-left.

(a)

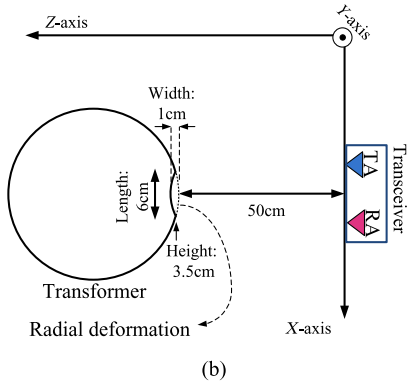

(b)

Fig. 17. Concave radial deformation (a) image and (b) top view scheme.

the deformations are aligned with the movement direction of antennas and located in the middle and top parts of the winding, respectively.

To show the capability of the proposed ideas, the unaligned deformations are also examined by the 12-section strategy. The bottom-right deformation is 30° to the right side as shown in Fig. 8(b). Fig. 15 demonstrates the results of 12-section strategy for this test case which indicates the capability of the proposed ideas to locate the deformations even if they are not in front of the imaging axis. The top-left deformation is 30° to the left side as shown in Fig. 8(b). Fig. 16 demonstrates the results of 12-section strategy for this test case.

VI. Actual Radial Deformation Detection

In the previous sections, the ability of the proposed method in locating modeled radial deformations on the actual transformer winding was investigated. The modeled deformation had a bulgy form, as shown in Fig. 5. However, the actual mechanical defects on power transformer windings may have different shapes and dimensions. First, these defects may occur in the shape of some concave buckling on the transformer winding. Second, the width of these defects can be less than that of the modeled deformation. Hence, to obtain more realistic results, a radial concave buckling is made on the winding. Fig. 17 presents the related picture and the top view scheme. As illustrated in this figure, the radial deformation is in the top

TABLE VI
RESULTS OF ACTUAL BUCKLING DEFORMATION BY "TWO-SECTION" STRATEGY

Cases		N_{warm}	S_{warm}
Deformation on top part	Upper section	**54853**	**29567**
	Lower section	64845	36124

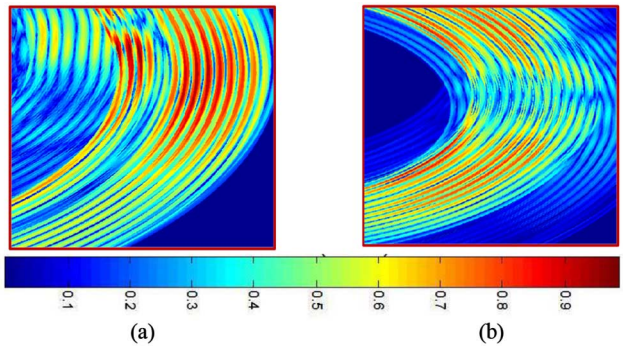

Fig. 18. "Two-section" strategy applied on imaging data of winding when actual buckling mechanical deformation is on top part. (a) Lower section. (b) Upper section.

section of the HV winding. The same vertical setup has been used for the imaging. Unlike the bulgy deformation in previous sections, the concave shape of the deformation causes a longer distance between antennas and the winding in the deformation location. Therefore, it is expected to have less hot colors in that place in the resulted images. This fact can be observed from the data in Tables III and VI.

The two-section strategy is used to detect the deformation location. Lower N_{warm} and S_{warm} parameters indicate the section in which the buckling deformation has been occurred. Table VI presents the obtained parameters. As shown, both N_{warm} and S_{warm} are less for upper section in which the deformation is occurred. Also, it should be considered that this deformation width is %40 of the previous modeled one. However, it is successfully detected using the proposed imaging method which demonstrates the effectiveness of this method in detecting different shapes and dimensions of mechanical deformations. In Fig. 18, it is illustrated that hot colors in the upper section are less than those in the lower section. Also, the deformation has made some disconnections in the lines of the upper section due to its concave shape.

To obtain more accurate results, the 12-section strategy is also applied in this test case. Fig. 19 shows that in the top part, specially 10th and 11th parts, N_{warm} and S_{warm} are lowest, which illustrate the presence of a buckling deformation in theses sections. Apparently, the accuracy is increased in comparison to the last two-section strategy in which only the defected half of the winding could be detected.

VII. DISCUSSION

The proposed imaging, migration algorithm, and image processing methods intend to detect deformations of transformers in an online manner which is very important for future smart applications. Also, the final industrial prototype should be capable to be implemented on three-phase transformers.

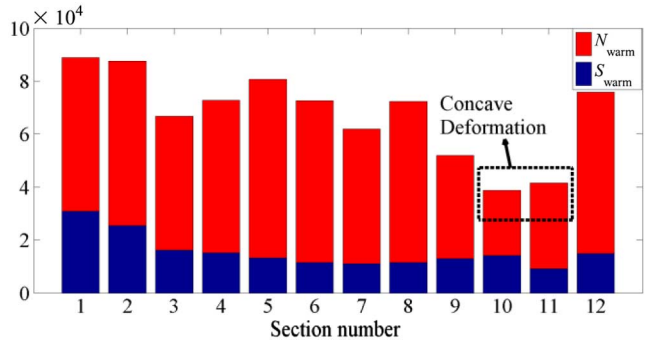

Fig. 19. "12-section" strategy results for actual buckling deformation on top.

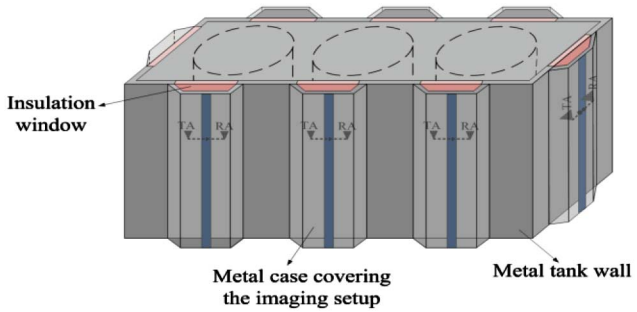

Fig. 20. Typical three-phase transformer with eight imaging setups and corresponding insulation windows.

Therefore, authors emphasize the practicability of the proposed methods. Fig. 20 shows a typical three-phase transformer with imaging setups and corresponding insulation windows. Insulation windows should be implemented on each side of the transformer tank (by cutting some parts of the tank and covering them by insulation materials) to make the imaging process possible. Then, the antennas should be located in front of these windows. The electromagnetic waves easily pass through the insulator, reach the transformer winding, and reflect back to the antenna. This technique has been successfully implemented for the partial-discharge monitoring of power transformers, using ultra-high-frequency (UHF) sensors [24]. Polytetrafluoroethylene (PTFE) or filled epoxy resin insulators have been tested in [24] as materials to be used as insulation windows. Also, the effects of two different insulators in radar imaging have been tested in our laboratory. One of them is glass and the other one is polymer. However, investigating on the exact setup specifications, their optimum and accurate sizes, and their accuracy in the case of a three-phase transformer are possible future work. The application of this method on a real transformer necessitates further investigation to take into consideration the effects of "insulation oil," "tank," etc. Therefore, authors emphasize that the tests on the effects of modeled metal tank and oil existing around the winding have been successfully done in our laboratory. As stated earlier, existence of the insulation material around the winding provides the practicability of the imaging process. It is worth mentioning that application of the proposed image processing method eliminates the effect of the metal tank around transformer winding. Since the tank effect around the windings is permanently constant, its reflections in both sound and defected images are

the same. Therefore, the result of this reflection will be removed when the correlation is calculated between the sound and other images.

The distance between the transformer winding and the SAR imaging setup only changes the round trip time of the signal, and it does not affect the accuracy and final results. Therefore, considering the fact that once a setup is properly installed outside of a transformer tank, the distance will remain constant, and authors believe that the proposed ideas can be practically applied on a real power transformer with adapted sizes (close to the applied distances in our paper).

Considering the effects of background noises, harmonics, switching operations, and nearby radio frequencies on the imaging performances, followings are some possibilities to get rid of these problems. First of all, the working frequency of UWB antennas is about 5 GHz. Therefore, "harmonics" and "switching" frequencies, which exist inside the tank, are far from this gigahertz range and will not affect imaging operation. However, radio frequencies and high-frequency noises existing around the transformer tank can be prohibited to be entered into the imaging environment by putting the imaging setup inside the metal cases made up of the materials similar to that of the transformer tank. These metal cases can be visualized as shown in Fig. 20. The monitoring of the transformer (especially the three-phase one) can be done step by step, and at each step, one side of the transformer can be monitored. There is no need to monitor all sides of the transformer at exactly the same time. This is useful in terms of avoiding antennas interferences and more importantly it is cost effective (because only one imaging setup can be used). On the other hand, in the case of using more than one imaging setup simultaneously, time-gating method can solve the interference problems. Using time-gating method, the undesired part of the received data will be removed and only the target data will be processed. The main goal of this paper is trying to propose useful ideas for the online and smart monitoring of future transformers. However, it is possible to apply the proposed methods on the current in-service transformers if the insulation windows can be created on their tank (e.g., on those transformers which are disconnected for maintenance or change). This paper focused to monitor and find the location of "radial deformations" using image processing approaches. However, applying similar image processing methods and ideas on other mechanical deformations such as axial displacement and disc space variation can be done as future work. SAR imaging provides useful data with a moderate data size. These data can be quickly processed using migration algorithm to obtain the images, as described earlier. Due to the costs of expensive transformers, huge repair/maintenance, and failure costs, monitoring and metering of these deformations especially in an online manner are (and will be) very interesting for the current industry (and future smart grids). Therefore, authors believe that the proposed ideas will be practically useful and adopted by the industry. A simple camera is useless due to the existence of the insulation windows (made up of polymer or PTFE) and the transformer oil between the target and imaging setup. On the other hand, the obtained data size from SAR imaging and its quantized interpretations are well suited with our purpose and they are not comparable with large sizes of images taken by simple camera requiring a huge burden of processing and computation. Because of these two reasons, the simple camera is useless for our purposes.

There are different ways to interpret SAR images and transfer them into quantitative values. One way is to use N_{warm} and S_{warm} which differentiate the colors into warmer and colder colors with only a certain value. This method of transferring the image to quantitative values has some merits such as simplicity and fastness for distinguishing between the sound and radially deformed images and detecting the location of normal radial deformations. However, as illustrated in the experimental results, the accuracy of using S_{warm} in Figs. 13, 16, and 19 is not as high as using that in Figs. 12, 14, and 15. Furthermore, its accuracy is not as high as the accuracy of using the N_{warm} index in Figs. 13, 16, and 19. Another way to interpret the images and transfer them into quantitative values is to use histogram notion instead of just defining the warm and cold colors, e.g., having lots of color intervals. This method of quantifying has some useful advantages such as carrying more information which can be used to detect the location of other types of deformations, very small radial deformations, or radial deformations with less favorable locations in a more accurate manner. Therefore, it can be a good future work in this area. However, to detect the location of the normal radial deformations presented in this paper, the accuracy of both methods will be almost the same. Because, the accuracy of the image processing strategies proposed in this paper profoundly depends on the number of imaging points shown in Fig. 4(b) and it is not considerably affected by the number of color bar divisions. On the other hand, high-division method (or histogram notion) carries some disadvantages comparing to its two-division counterpart proposed in this paper, e.g., it is harder to interpret normal radial deformations, and it needs more calculation and processing burdens.

VIII. Conclusion

In this paper, the application of image processing methods for detecting the presence and location of mechanical deformations on an actual transformer winding has been studied. The winding images have been obtained using the SAR imaging method and KM algorithm. Three-stage image processing strategies have been proposed and applied on the experimental setup. The results show that the first and second stages are capable in detecting the presence and type of the deformation. Also, the results of the third stage (n-section strategies) indicate that the location of the different deformations is successfully detected. Moreover, the bulgy modeled mechanical deformation has been substituted with an actual concave deformation with smaller size on the winding, and the imaging process has been repeated. The results show that the proposed ideas can properly locate this deformation too.

Acknowledgment

The authors would like to thank Dr. M. A. Hejazi, Mr. M. S. Golsorkhi, and Mr. H. Karami for their help in the laboratory, and suggestions and comments.

REFERENCES

[1] J. You, S. Yin, and H. Gao, "Fault detection for discrete systems with network-induced nonlinearities," *IEEE Trans. Ind. Informat.*, vol. 10, no. 4, pp. 2216–2223, Nov. 2014.

[2] O. Geramifard, J.-X. Xu, J.-H. Zhou, and X. Li, "A physically segmented hidden Markov model approach for continuous tool condition monitoring: Diagnostics and prognostics," *IEEE Trans. Ind. Informat.*, vol. 8, no. 4, pp. 964–973, Nov. 2012.

[3] J. Antonino-Daviu, S. Aviyente, E. G. Strangas, and M. Riera-Guasp, "Scale invariant feature extraction algorithm for the automatic diagnosis of rotor asymmetries in induction motors," *IEEE Trans. Ind. Informat.*, vol. 9, no. 1, pp. 100–108, Feb. 2013.

[4] M. D. Naso, B. Turchiano, and P. Pantaleo, "A fuzzy-logic based optical sensor for online weld defect-detection," *IEEE Trans. Ind. Informat.*, vol. 1, no. 4, pp. 259–273, Nov. 2005.

[5] H. Gao, C. Ding, C. Song, and J. Mei, "Automated inspection of E-shaped magnetic core elements using K-tSL-center clustering and active shape models," *IEEE Trans. Ind. Informat.*, vol. 9, no. 3, pp. 1782–1789, Aug. 2013.

[6] J. Seshadrinath, B. Singh, and B. K. Panigrahi, "Vibration analysis based interturn fault diagnosis in induction machines," *IEEE Trans. Ind. Informat.*, vol. 10, no. 1, pp. 340–350, Feb. 2014.

[7] M. Drif and A. J. M. Cardoso, "Stator fault diagnostics in squirrel cage three-phase induction motor drives using the instantaneous active and reactive power signature analyses," *IEEE Trans. Ind. Informat.*, vol. 10, no. 2, pp. 1348–1360, May 2014.

[8] H. Karami, M. S. A. Hejazi, M. S. Naderi, G. B. Gharehpetian, and S. Mortazavian, "Three-dimensional simulation of PD source allocation through TDOA method," in *Proc. 4th Conf. Therm. Power Plants (CTPP)*, Dec. 2012, pp. 1–4.

[9] Z. Sahri, R. Yusof, and J. Watada, "FINNIM: Iterative imputation of missing values in dissolved gas analysis dataset," *IEEE Trans. Ind. Informat.*, vol. 10, no. 4, pp. 2093–2102, Nov. 2014.

[10] S. Mortazavian, G. B. Gharehpetian, M. A. Hejazi, M. S. Golsorkhi, and H. Karami, "A simultaneous method for detection of radial deformation and axial displacement in transformer winding using UWB SAR imaging," in *Proc. 4th Conf. Therm. Power Plants (CTPP)*, Dec. 2012, pp. 1–6.

[11] M. S. Golsorkhi, M. S. A. Hejazi, G. B. Gharehpetian, and M. Dehmollaian, "A feasibility study on the application of radar imaging for the detection of transformer winding radial deformation," *IEEE Trans. Power Del.*, vol. 27, no. 4, pp. 2113–2121, Oct. 2012.

[12] M. Bagheri, M. S. Naderi, and T. Blackburn, "Advanced transformer winding deformation diagnosis: Moving from off-line to on-line," *IEEE Trans. Dielectr. Elect. Insul.*, vol. 19, no. 6, pp. 1860–1870, Dec. 2012.

[13] M. S. Naderi, G. Gharehpetian, M. Abedi, and T. Blackburn, "Modeling and detection of transformer internal incipient fault during impulse test," *IEEE Trans. Dielectr. Elect. Insul.*, vol. 15, no. 1, pp. 284–291, Feb. 2008.

[14] D. M. Sofian, Z. Wang, and J. Li, "Interpretation of transformer FRA responses—Part II: Influence of transformer structure," *IEEE Trans. Power Del.*, vol. 25, no. 4, pp. 2582–2589, Oct. 2010.

[15] M. M. Shabestary, A. J. Ghanizadeh, G. B. Gharehpetian, and M. Agha-Mirsalim, "Ladder network parameters determination considering non-dominant resonances of the transformer winding," *IEEE Trans. Power Del.*, vol. 29, no. 1, pp. 108–117, Feb. 2014.

[16] W. Portilla, G. Mayor, J. Guerra, and C. Gonzalez-Garcia, "Detection of transformer faults using frequency-response traces in the low-frequency bandwidth," *IEEE Trans. Ind. Electron.*, vol. 61, no. 9, pp. 4971–4978, Sep. 2014.

[17] A. Siada and S. Islam, "A novel online technique to detect power transformer winding faults," *IEEE Trans. Power Del.*, vol. 27, no. 2, pp. 849–857, Apr. 2012.

[18] K. Song and Q. Xue, "Ultra-wideband ring-cavity multiple-way parallel power divider," *IEEE Trans. Ind. Electron.*, vol. 60, no. 10, pp. 4737–4745, Oct. 2013.

[19] F. Costa, E. Laboure, F. Forest, and C. Gautier, "Wide bandwidth, large ac current probe for power electronics and EMI measurements," *IEEE Trans. Ind. Electron.*, vol. 44, no. 4, pp. 502–511, Aug. 1997.

[20] S. Pramanik and L. Satish, "Localisation of discrete change in a transformer winding: A network-function-loci approach," *IET Elect. Power Appl.*, vol. 5, no. 6, pp. 540–548, 2011.

[21] R. L. Moses and J. N. Ash, "An autoregressive formulation for SAR back projection imaging," *IEEE Trans. Aerosp. Electron. Syst.*, vol. 47, no. 4, pp. 2860–2873, Oct. 2011.

[22] X. Zhuge, A. Yarovoy, T. Savelyev, and L. Ligthart, "Modified Kirchhoff migration for UWB MIMO array-based radar imaging," *IEEE Trans. Geosci. Remote Sens.*, vol. 48, no. 6, pp. 2692–2703, Jun. 2010.

[23] J. W. Goodman, *Introduction to Fourier Optics*. Greenwood Village, CO, USA: Roberts and Company, 2005, pp. 39–55.

[24] M. D. Judd, L. Yang, and I. B. B. Hunter, "Partial discharge monitoring of power transformers using UHF sensors part 2: Sensors and signal interpretation," *IEEE Elect. Insul. Mag.*, vol. 21, no. 2, pp. 5–14, Mar./Apr. 2005.

Shahed Mortazavian (S'15) received the B.Sc. degree from the Isfahan University of Technology, Isfahan, Iran, and the M.Sc. degree from the Amirkabir University of Technology, Tehran, Iran, in 2007 and 2013, respectively, both in electrical engineering. She is currently pursuing the Ph.D. degree in electrical and computer engineering at the University of Alberta, Edmonton, AB, Canada.

From 2007 to 2011, she was a Senior Engineer with Pardisan Engineering Co., Isfahan, working on different industrial, research and development projects in the field of design and implementation of supervisory control and data acquisition (SCADA) and digital control systems. Her research interests include dynamics of power converters, power systems and micro-grids stability, renewable generations, and fault diagnosis and condition monitoring in power systems.

Masoud M. Shabestary (S'14) received the B.Sc. degree in electrical engineering from the Amirkabir University of Technology (Tehran Polytechnic), Tehran, Iran, in 2011, and the M.Sc. degree in energy systems from the University of Alberta, Edmonton, AB, Canada, in 2015. He is currently pursuing the Ph.D. degree in electrical engineering at the University of Alberta.

From 2011 to 2013, he served as a Research Assistant with the Flexible AC Transmission Systems Laboratory, Amirkabir University of Technology. His research interests include renewable and sustainable energies; distributed generation units and their analysis, control, and protection; application of power electronics in smart/micro grids; and condition monitoring of electrical equipment.

Yasser Abdel-Rady I. Mohamed (M'06–SM'11) was born in Cairo, Egypt, in 1977. He received the B.Sc. (Hons.) and M.Sc. degrees from Ain Shams University, Cairo, Egypt, in 2000 and 2004, respectively, and the Ph.D. degree from the University of Waterloo, Waterloo, ON, Canada, in 2008, all in electrical engineering.

He is currently an Associate Professor with the Department of Electrical and Computer Engineering, University of Alberta, Edmonton, AB, Canada. His research interests include dynamics and controls of power converters; distributed and renewable generation and microgrids; modeling, analysis, and control of smart grids; and electric machines and motor drives.

Dr. Mohamed is a registered Professional Engineer in the Province of Alberta. He is an Associate Editor of the IEEE TRANSACTIONS ON INDUSTRIAL ELECTRONICS. He is also a Guest Editor of the IEEE TRANSACTIONS ON INDUSTRIAL ELECTRONICS Special Section on Distributed Generation and Micro-Grids.

Gevork B. Gharehpetian received the B.S. degree from Tabriz University, Tabriz, Iran, in 1987; the M.S. degree from the Amirkabir University of Technology (AUT), Tehran, Iran, in 1989; and the Ph.D. degree from Tehran University, Tehran, in 1996, all with First Class Honors and all in electrical engineering.

He was an Assistant Professor with AUT, from 1997 to 2003; an Associate Professor from 2004 to 2007; and has been a Professor since 2007. He is a Member of the Power Engineering Group at AUT, which has been selected as a Center of Excellence on Power Systems in Iran since 2001. His research interests include power system and transformers transients, and power electronics applications in power systems.

Dr. Gharehpetian was selected by the Ministry of Higher Education as a Distinguished Professor of Iran, and by the Iranian Association of Electrical and Electronics Engineers (IAEEE) as a Distinguished Researcher of Iran, and was awarded the National Prize in 2008 and 2010, respectively.